Available online at www.sciencedirect.com

ScienceDirect

Journal of the European Ceramic Society 34 (2014) 4247–4256

www.elsevier.com/locate/jeurceramsoc

Textured Al-doped ZnO ceramics with isotropic grains

P. Díaz-Chao [a], F. Giovannelli [b,*], O. Lebedev [a], D. Chateigner [a,c], L. Lutterotti [a], F. Delorme [b], E. Guilmeau [a]

[a] *CRISMAT, UCBN, ENSICAEN, 6 Boulevard du Maréchal Juin, 14050 Caen Cedex, France*
[b] *Université François Rabelais de Tours, CNRS, CEA, INSA, GREMAN UMR 7347, IUT de Blois 15 rue de la chocolaterie, 41029 Blois Cedex, France*
[c] *IUT-Caen, Université de Caen Basse-Normandie, 6 Boulevard du Maréchal Juin, 14050 Caen Cedex, France*

Received 23 April 2014; received in revised form 3 July 2014; accepted 7 July 2014
Available online 24 July 2014

Abstract

Pure ZnO and single Al-doped ZnO compounds without secondary phase have been obtained by SPS process. Starting powders prepared by co-precipitation have been synthesized. The sintered pellets exhibit different texture degree but similar isotropic shaped grains. Sintering mechanisms are proposed for both powders, explaining the different texture and grain size evolutions as a direct consequence of the differences observed in both compounds. The influence of texture and grain morphology on the thermoelectric properties is studied.

Keywords: Spark plasma sintering; Thermoelectric properties; Texture; Anisotropy

1. Introduction

ZnO is a non-toxic, biocompatible, abundant, transparent oxide which has attracted much attention for a large number of applications due to its varied properties.[1–3] It presents a wide band gap of 3.3 eV in which different energy levels introduced by O and Zn defects are probably responsible for the electrical conductivity in pure ZnO.[4] Many authors have already reported the enhancement of the transport properties of ZnO motivated by its potential application in fields such as photovoltaic[5,6] or thermoelectric energy conversion.[7–10] To this aim, pure ZnO has been doped with several elements such as Al,[7,8,10,11] Ga,[12] Ni[13,14] or P.[15,16] The addition of metal oxides like Bi_2O_3, CoO, MnO, or Sb_2O_3, has also been investigated for its use in varistors.[17]

ZnO has been prepared in the form of 1D nanotubes, whiskers or nanorods by pulsed laser ablation (PLD), electrochemistry, chemical vapour deposition (CVD) or thermal evaporation.[18–23] It has also been prepared in 2D thin films using CVD, MOCVD, PLD and electrochemistry, among others,[24–27] as well as in 3D polycrystalline powders and single crystals. The most common procedure to prepare bulk polycrystalline ZnO is to use some chemical route, and compact it afterwards by techniques like conventional sintering, hot pressing, or spark plasma sintering (SPS).[4,12,28] Among these techniques, the SPS presents the advantage of achieving high densities at lower temperatures than with the other techniques.[29] This is particularly interesting for nano-sized powder elaboration since nanometric grain sizes can be preserved, as well as to avoid volatilization of Zn.

ZnO crystallizes in two different polymorph structures, cubic zincblende and hexagonal wurzite. The zincblende-ZnO is the less common form because of its metastable character at ambient conditions. Nevertheless, some of its properties like its ability to alloy with MgO for bandgap engineering[30] or its role in the formation of ZnO nanostructures[31] makes its study increasingly attractive. The wurzite-type, on the other hand, is the stable form of the ZnO at ambient conditions and has been much more commonly used and studied. The hexagonal structure of the wurzite gives an anisotropic character that has been rarely studied in bulk[32–34] and more extensively in the form of thin films.[26,35] In the case of ZnO bulks elaborated by SPS, it appears that combining the SPS process with other anisotropic fields during sintering, like extrusion or high magnetic field, is necessary to

* Corresponding author. Tel.: +33 254552110.
E-mail address: fabien.giovannelli@univ-tours.fr (F. Giovannelli).

http://dx.doi.org/10.1016/j.jeurceramsoc.2014.07.009
0955-2219/

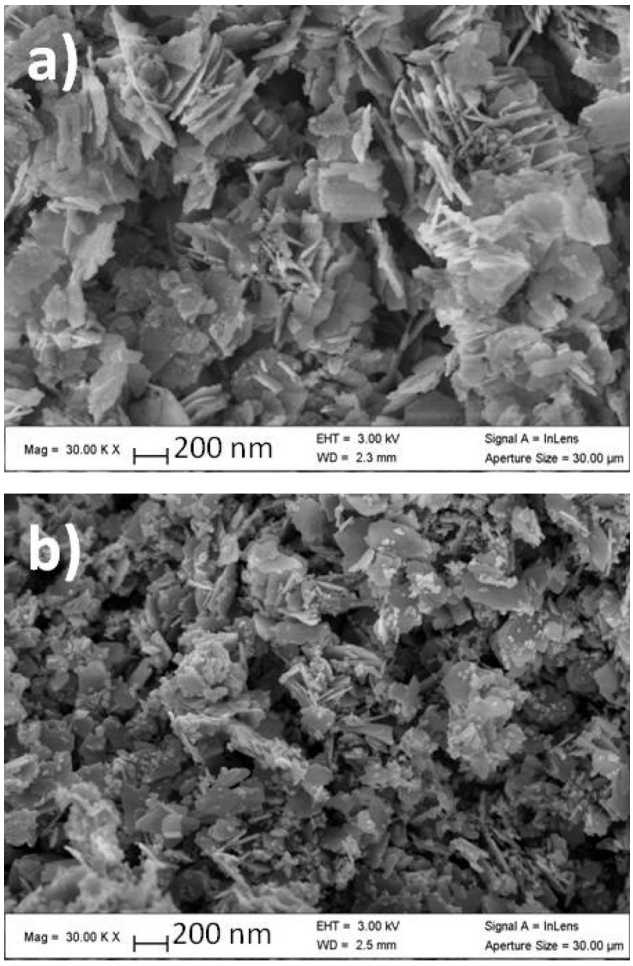

Fig. 1. SEM images of the (a) pure and (b) Al-doped ZnO starting powder.

achieve large preferred orientations.[32,33] These works resulted in elongated crystallites having their *c*-axis in the main direction of the particles.

In this work, we report the SPS formation of crystallized and oriented ZnO with isotropic grain morphology without using any external influence. The sintering process, the structure and microstructure of the samples are described along with its transport properties. A densification mechanism is proposed.

2. Experimental

100 ml of cationic solution have been obtained by dissolution of $Zn(NO_3)_2{\cdot}6H_2O$ (Aldrich 99.99%) and $AlCl_3$ (Acros 99%) in demineralised water. The Zn concentration is 1 M and in the case of doped sample Al concentration corresponds to 5 atomic percent of Zn. Precipitation has been performed by dropwise addition of 125 ml of a 4 M NaOH solution (solid NaOH from Scharlau (99%)) during 25 min. The precipitate thus obtained was centrifuged at 4000 rpm during 5 min and washed with distilled water. This step was repeated five times. The solid was finally dried at 80 °C.[36] In the case of aluminium doped samples laser ablation–inductively coupled plasma–mass spectrometry (LA-ICP-MS) analysis was performed. An elemental XR Thermo Specific, following the procedure described in

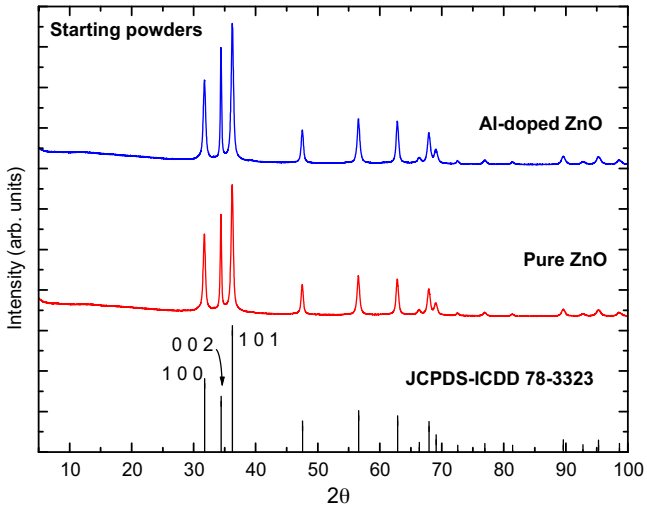

Fig. 2. XRD of pure and Al-doped ZnO starting powder.

previous studies[37–39] was used in combination with a VG UV laser probe laser ablation sampling device. Solid samples were prepared as pressed pellets. Powder samples of 350 mg were put under 8 metric tonne pressure, without added binder, to form 13 mm (diameter) × 1 mm (height) pellets. The repetition rate of the 266 nm wavelength laser was fixed to 10 Hz. Calibration took place with certified artificial glass, NIST-610. Measurements were replicated four times to validate the analytical precision of the technique.

Pure and Al-doped (0.3%) ZnO pellets have been prepared by spark plasma sintering (SPS) in a FCT model HPD25 at temperatures ranging from 600 °C to 1100 °C for pure ZnO and from 400 °C to 1000 °C for Al-doped ZnO in a graphite die. A dwell time of 5 min and a heating rate of 100 K/min have been used under an applied pressure of 100 MPa. The structural characterization of the powder source and of the pellets has been performed by X-ray diffraction (XRD) in a Philips X'pert pro MPD PANalytical diffractometer, using CuKα radiation. The XRD measurements after sintering were performed on the surface perpendicular to the SPS applied pressure (P_{SPS}) as well as on the cross section. Texture analysis was performed using a 4-circle diffractometer setup equipped with a Curved Position Sensitive detector (CPS120 from INEL SA) with monochromatic CuKα radiation.[40] Data were analyzed within the combined analysis formalism[41] implemented in the MAUD software.[42] The morphology of the samples before and after the sintering has been studied by scanning electron microscopy (SEM) in a field emission gun SEM model Carl ZEISS SUPRA 55. No metallization has been performed. TEM investigations were carried out with a Tecnai G2 30 UT microscope operated at 300 kV and having 0.17 nm point resolution. The TEM samples were prepared by crushing the powder in an agate mortar, dissolved in methanol and spread out on Cu carbon holey grid. Seebeck coefficient (S) and electrical resistivity (ρ) have been measured in a ULVAC ZEM-3 equipment by the differential and the four-probe point methods, respectively. The thermal diffusivity (α) has been obtained by the laser flash analysis technique in a Netzch LFA-457 equipment. Thermal conductivity (κ) was determined using

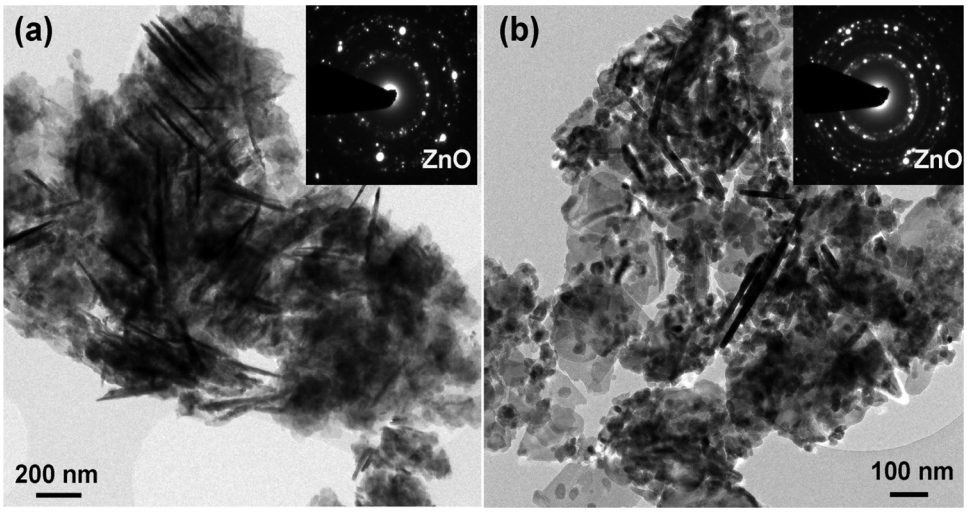

Fig. 3. TEM images of (a) pure and (b) doped ZnO powders.

the product of the geometrical density, the thermal diffusivity and the heat capacity. The heat capacity was calculated using the Dulong-Petit law.

3. Results

SEM images of pure and Al-doped ZnO starting powders (Fig. 1a and b, respectively) show platelet-like particles of irregular contours with a high aspect ratio, mean platelet sizes being larger in the Al-doped samples. Small round-shaped particles of ~20 nm in diameter can also be observed in the Al-doped powder. The corresponding XRD patterns of both doped and non-doped powders before SPS (Fig. 2), however, do not show any significant difference within the used instrumental resolution. The comparison of both diffractograms with the reference wurtzite pattern of ZnO ($P6_3mc$ space group, Crystallography Open Database no. 9004178)[43] shows a slight preferred orientation of the powders with a larger intensity of the 002 peak compared to a randomly oriented powder ($2\theta = 34.4°$). The TEM images of both powders (Fig. 3a and b) confirm the presence of platelet-like particles with a similar high aspect ratio and higher abundance of smaller round-shaped particles in the Al doped powder. In the latter, the presence of needle-like particles is also observed in the powder crystallized along the *c*-axis (Fig. 4). In spite of the apparently similar morphology of both powders from the SEM images, the platelets of the pure ZnO show an heterogeneous morphology with darker stripes within the platelets that coincide with protrusions seen on the edges (Fig. 5). This structure might correspond to other platelets connected perpendicularly or forming a flower-like structure, as it can be seen in the SEM images in Fig. 1a. In any case, these crystal habits exhibit single-crystalline diffraction behaviour (Fig. 5).

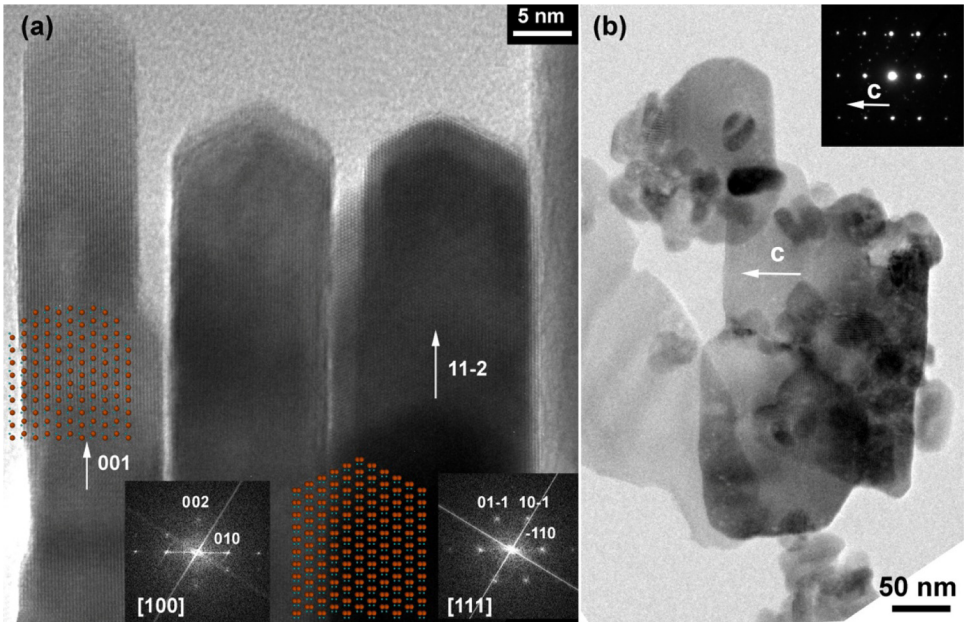

Fig. 4. TEM image of the Al-doped powder showing the crystallographic directions (a) in the needle-like and (b) in the platelet-like particles.

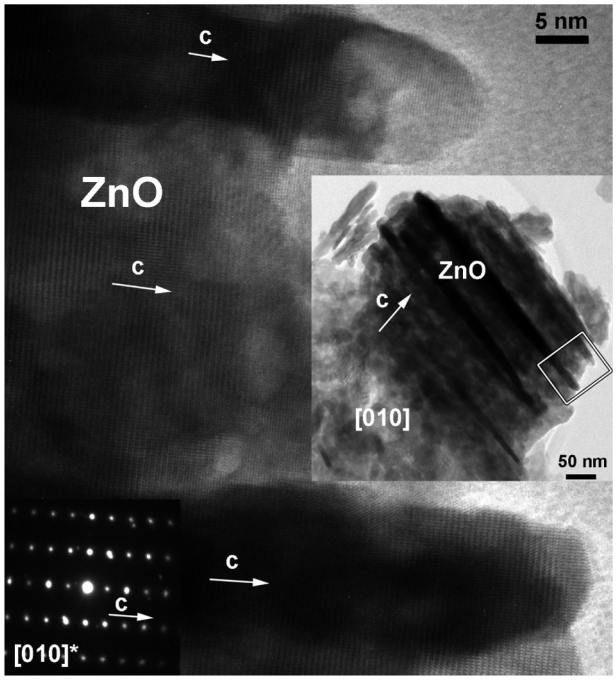

Fig. 5. TEM images of the pure ZnO powder. The main image corresponds to the area signalled by the square in the inset.

In the Al-doped powder, on the contrary, such structures are not observed. Platelet and needle-like particles are isolated from each others as seen by SEM and TEM (Figs. 1b and 4, respectively). On the one hand, it is important to note that in both powders the *c*-axis lies in the plane of the platelets, contrarily to platelet-like morphologies usually shown in the literature which exhibit their *ab*-plane as the platelet planes.[44,45] On the other hand, the crystallization of needle-like particles is usually obtained with the *c*-direction along the main axis of the particle,[45,46] as it is the case for the needles observed in this work.

After sintering, a density up to 99% is achieved in both doped and pure ZnO (Fig. 6a). However, both types of powders show different densification kinetics (Fig. 6b). Doped ZnO follows a simple sigmoid curve reaching densities higher than 90% at 500 °C, while a two shrinkage process is activated in the densification of the pure ZnO. The first shrinkage starts almost at room temperature and gives rise to densities up to ~70% at 400 °C, while the second one begins around 850 °C with a density of 99% at a temperature of 1100 °C.

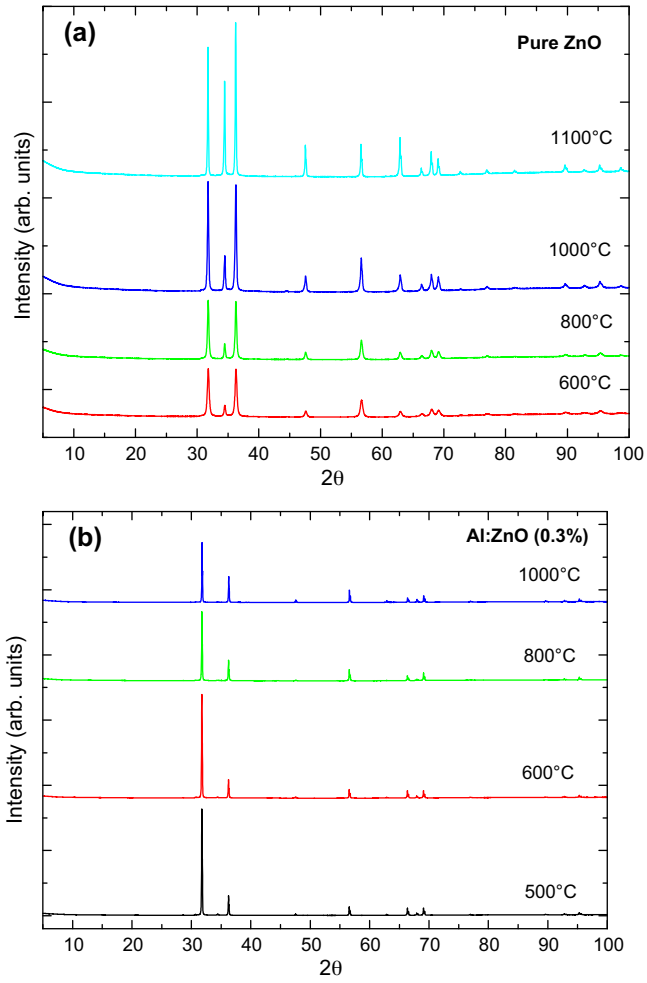

Fig. 7. X-ray diffractograms of (a) pure and (b) Al-doped samples performed on the surface perpendicular to the pressure axis.

The SPS process accomplishes sintered pellets with ZnO (doped or not) as the unique crystallized phase (Fig. 7a and b). This is consistent with the used low Al content which is probably below the solubility limit.[10,47] Indeed, previous studies showed

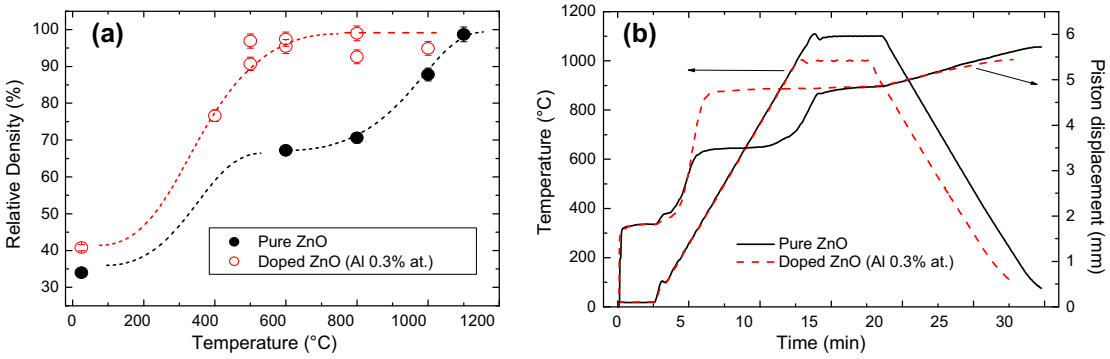

Fig. 6. (a) relative density of the Al-doped (red open circles) and pure (black solid circles) SPS-processed ZnO. Dotted lines are guides for the eye. (b) Temperature-time and piston displacement profiles for Al-doped (dashed lines) and pure (solid lines) ZnO. (For interpretation of the references to color in this figure legend, the reader is referred to the web version of the article.)

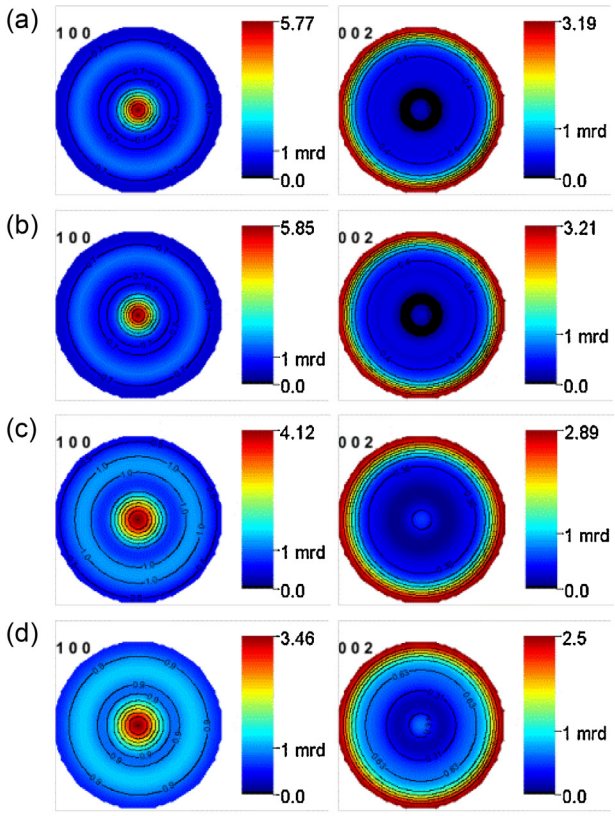

Fig. 8. Texture analysis measurement preformed on the Al-doped ZnO sintered at (a) 500 °C, (b) 600 °C, (c) 800 °C, and (d) 1000 °C.

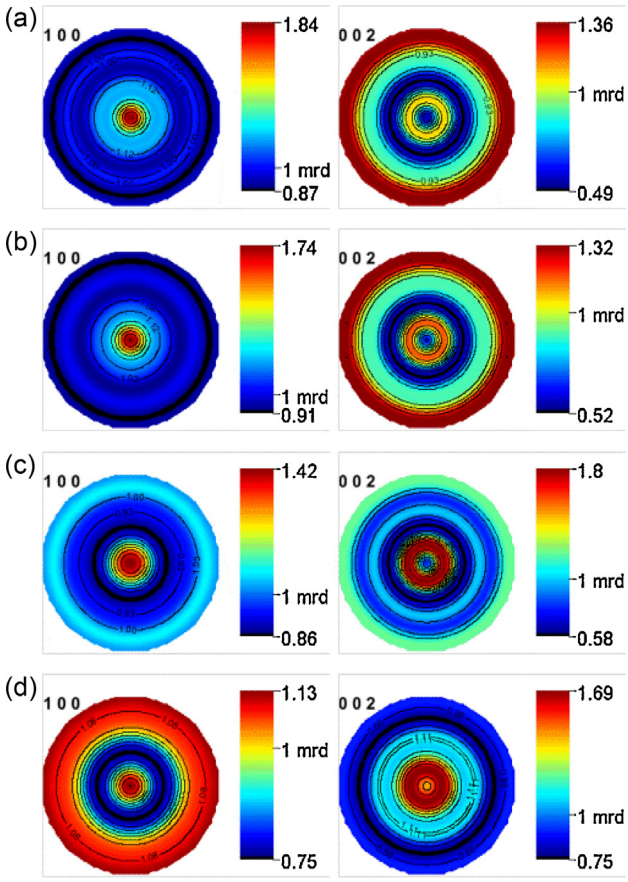

Fig. 9. Pole figures obtained with the MAUD software from standard XRD measurements performed on pure ZnO prepared at (a) 600 °C, (b) 800 °C, (c) 1000 °C, and (d) 1100 °C.

the apparition of secondary phases at grain boundaries when the aluminium content was larger than 1%at.[35,48] Moreover, the absence of the 0 0 2 diffraction peak ($2\theta = 34.43°$) in all the Al-doped samples indicates a significant texture in the resulting pellet. In the case of pure ZnO a preferential orientation can also be observed from the different relative intensity of the three main peaks (1 0 0 ($2\theta = 34.43°$), 2 0 0 ($2\theta = 34.43°$), and 1 0 1 ($2\theta = 34.43°$) with respect to the reference pattern. Furthermore, such relative intensities change with the sintering temperature, which indicates an evolution of the texture. A quantitative analysis of the texture of our samples has been then carried out by refining the XRD diffractograms using the Combined Analysis approach.[41] The Orientation Distribution Function (ODF) was refined using spherical harmonics integrated during the Rietveld fit of the diagrams in the MAUD software.[42] From the ODF the pole figures for the main directions {1 0 0} and {0 0 2} (Figs. 8 and 9) were calculated.

According to the {1 0 0} and {0 0 2} pole figures of Al-doped samples, pole density maxima are obtained for the directions parallel and perpendicular to P_{SPS} respectively. The orientation density reinforcement of the equator of the {0 0 2} pole figure clearly indicates a preferred alignment of the *c*-axes perpendicular to the pressure direction. This preferred orientation is maintained over the whole temperature range, but its magnitude decreases as the sintering temperature increases, with {0 0 2} pole density maxima going from 3.2 mrd down to 2.5 mrd. The pure ZnO samples exhibit a comparatively weaker texture. As in the case of the doped samples, the pure ZnO samples sintered at the lowest temperatures (600 °C and 800 °C) show orientation density maxima in {1 0 0} and {0 0 2} pole figures for the directions parallel and perpendicular to P_{SPS}, respectively. However, in the samples prepared at higher temperatures (1000 °C and 1100 °C), the orientation density behaviour reverses, with {0 0 2} pole figure maxima found in the direction parallel to P_{SPS}, though the orientation density along this direction is still lower than in doped samples (not larger than 1.8 mrd).

It is worth noting that the observed crystallographic preferred orientations are not obvious in the SEM images of the surface and the cross-section of our sintered compounds, as seen in Al-doped sample sintered at 500 °C (Fig. 10). Neither hexagonal-shape can be seen on the cross section nor elongated shapes on the surface, and rather isotropic shapes can be seen for all the temperature range in the Al-doped samples (Fig. 11) as well as in the pure ZnO samples sintered at 1000 °C and 1100 °C (Fig. 12). Only in the samples of pure ZnO sintered at lower temperatures (600 °C and 800 °C) some grain shape anisotropy still is present.

The evolution of the grain size of the Al-doped and pure samples can also be seen in Figs. 11 and 12, respectively. The grain size of Al-doped samples increases more significantly than in the case of pure ZnO where the grain growth is observed mainly in the samples obtained at 1000 °C and 1100 °C. This

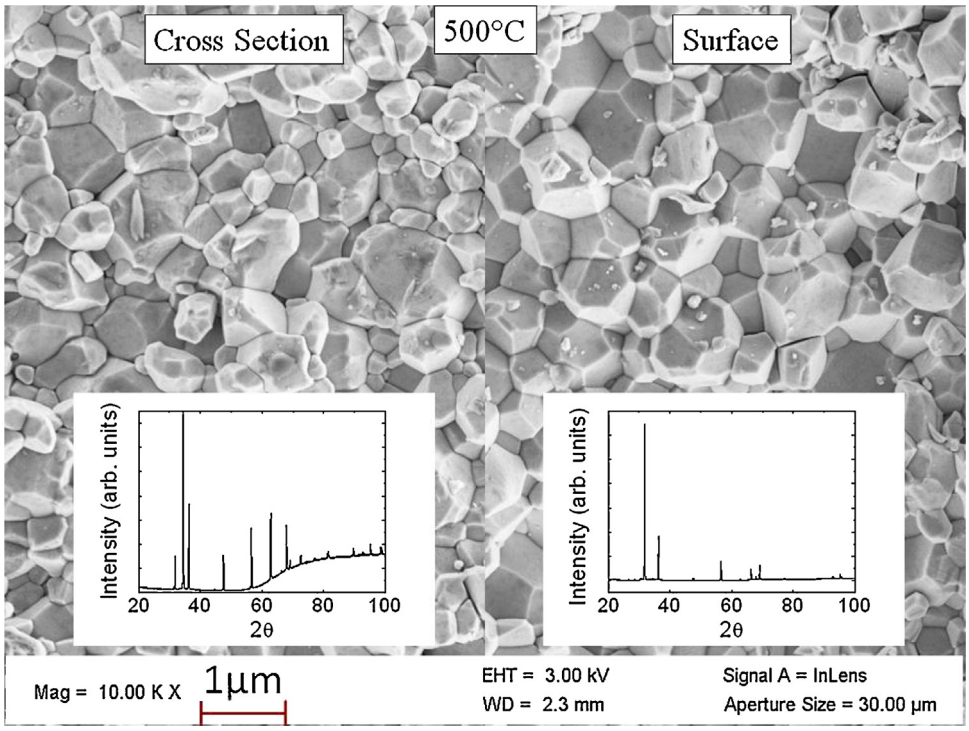

Fig. 10. SEM image of the surface and the cross section of an Al-doped sample sintered at 500 °C. The X-ray diffractograms of the surface and cross section are also shown together with their corresponding SEM image.

grain size increase in Al-doped samples is also observed as much sharper diffraction peaks (compare Fig. 7b and a) in these latter.

The Seebeck, resistivity, and thermal diffusivity of the Al-doped sample sintered at 800 °C have been measured in the directions parallel and perpendicular to P_{SPS} (Fig. 13). The Seebeck and the thermal diffusivity of both directions present the same values within the measurement errors. The electrical resistivity, however, shows different values for the two directions, being more resistive along P_{SPS} at least up to around 400 °C. This anisotropy in resistive behaviour reduces with temperature

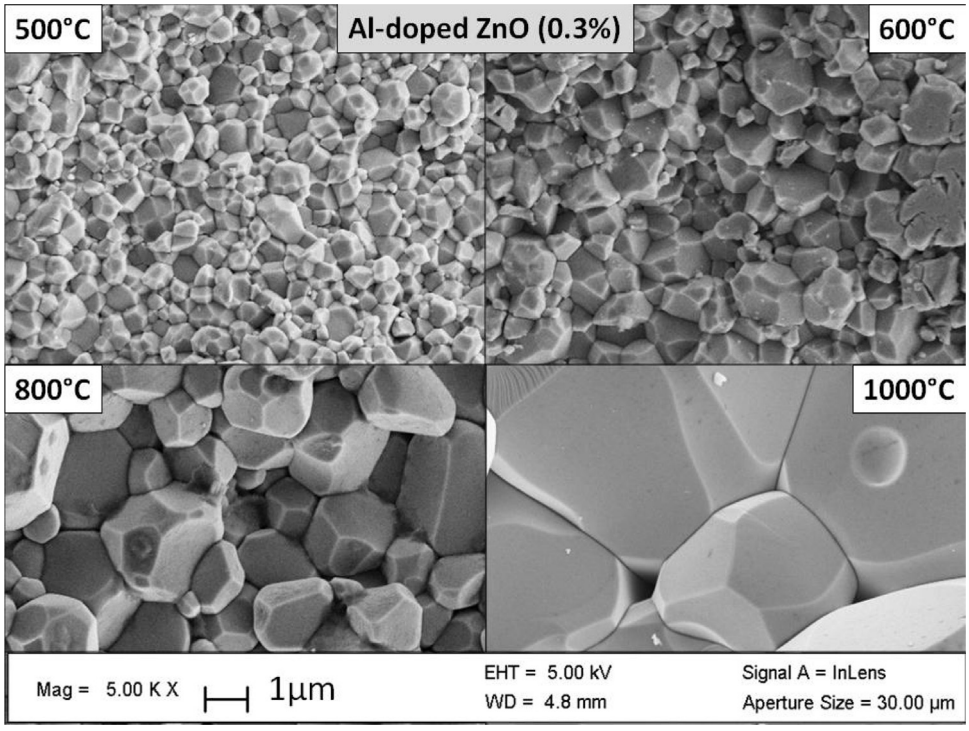

Fig. 11. Microstructure of the Al-doped ZnO samples obtained at 500 °C, 600 °C, 800 °C and 1000 °C.

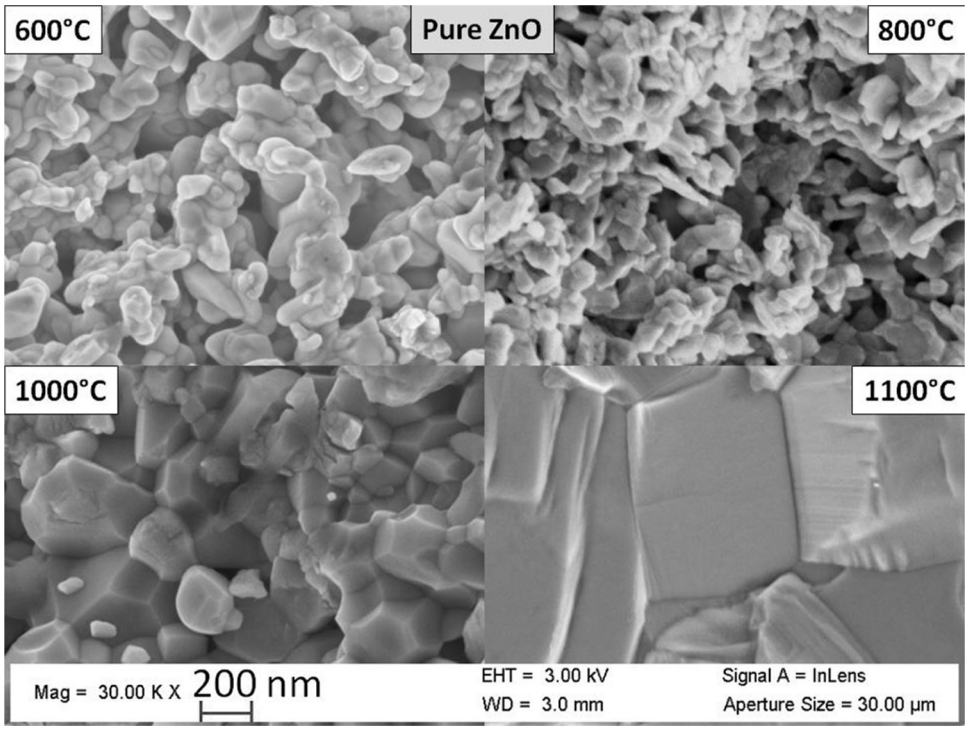

Fig. 12. Microstructure of the pure ZnO samples obtained at 600 °C, 800 °C, 1000 °C and 1100 °C.

and becomes negligible from 400 °C, up to 700 °C within the experimental errors.

4. Discussion

The texture stabilized in the sintered samples, with c axes preferentially oriented in the plane perpendicuar to P_{SPS}, can be easily understood as a direct consequence of the morphology of the starting powders, i.e. individual single crystal platelets with c axes in the plane rotate under an uniaxial pressure field to adopt a perpendicular orientation. However, even though the starting powders in both cases show the same XRD patterns with similar morphologies, the observed texture after sintering is clearly different, especially at high temperatures. Textured samples from co-precipitated powders has also been reported by Sondegaard et al.,[44] using ZnO powders with different morphologies. It was shown that powders synthesized by co-precipitation, which were formed by platelet-like particles, gave rise to the most intense preferred orientations among the different types of pure ZnO powders used. However, in their case, the platelets were found with a- and b-directions in the platelets plane, and correspondingly the *c*-axes aligned parallel to the pressure axis in the sintered samples. This difference probably arose from different elaboration conditions. Indeed, it is known that the morphology of the particles of ZnO prepared by co-precipitation depend strongly on experimental parameters as temperature, pH, or dosification.[46]

Remarkably, the grain morphology shown by the sintered Al-doped samples does not exhibit a lamellar shape, while existing for the precursor powder, but a more spherical-like one at all the temperatures, and with the same texture type with main c axes alignment perpendicular to P_{SPS}. In this regard, it should be noted that the grain size of the Al-doped sample sintered at 500 °C is very similar to the size of the platelets (∼200 nm), implying that the densification process of the Al-doped ZnO should have necessarily involved the widening of the platelets in the directions perpendicular to the *c*-axis, i.e. perpendicular to the original platelets.

Also, the shrinkage evolution of the pure ZnO pellets presents a second step above 850 °C which is not seen in the shrinkage of Al-doped powders. To the best of our knowledge, this point has not been reported previously for pure ZnO. Nevertheless, the fact that pure ZnO shows a density of only 70% makes it expectable that another densification mechanism could be activated when increasing sufficiently the temperature. As already mentioned in the previous section, it is interesting to highlight that the grains of the pure ZnO samples sintered at 600 °C and 800 °C do not show a spherical-like shape as exhibited by the Al-doped samples, but more anisotropic and closer to the original platelet shape, especially in the sample sintered at 600 °C. The grain shapes obtained at temperatures after starting the second shrinkage step acquire their spheroid character in doped samples, but accompanied by a texture decrease for higher temperatures. This fact suggests that a similar sintering mechanism described for the Al-doped samples occurs in the second step, i.e., the growth of the platelets in the direction perpendicular to the *c*-axis. In this way, the larger misorientation of initial platelets with respect to P_{SPS} further weakens the texture strength compared to the Al-doped sinters and explains the quite random distribution of crystal orientations at higher temperatures, when the proposed grain growth in the

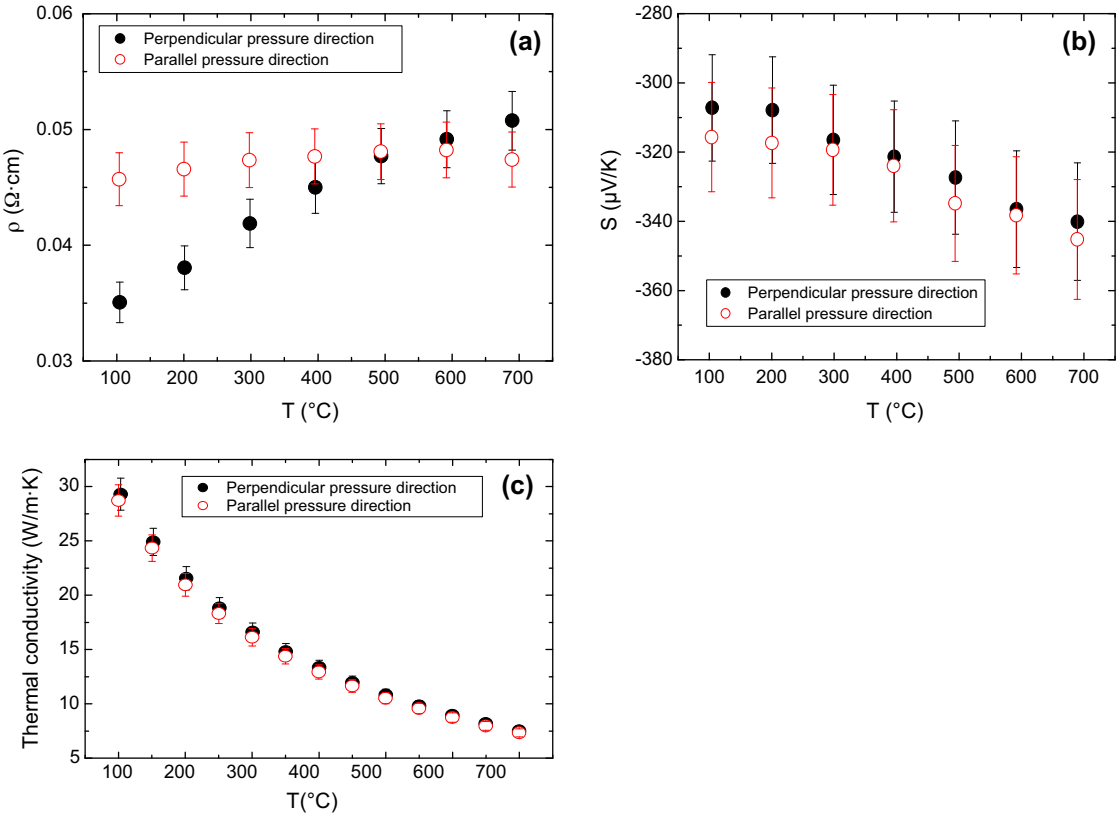

Fig. 13. (a) Electrical resistivity (ρ), (b) Seebeck coefficient (S), and (c) thermal conductivity of Al-doped ZnO in the parallel and perpendicular directions of the pressure.

direction perpendicular to the c-axis occurs. This randomization can be appreciated visually by comparing Fig. 2 (bottom diagram) and Fig. 7a (1100 °C, top diagram). Therefore, the differences shown in the shrinkage processes between the two kinds of samples, with different grain growth, shape and texture evolution, seem to arise from the different arrangement of the platelets in both powders. It is clearly observed in pure ZnO that platelet-like grains are connected among them perpendicularly and forming flower-like structures. These structures are missing in the Al-doped ZnO powder, what makes the stacking of the platelets easier, reaching higher orientation densities at lower temperatures, with c axes perpendicular to P_{SPS}, than in the case of the pure ZnO. This gives rise to larger powder densities for the same applied pressure, and to less texture loss with temperature during the process, in the Al-doped samples. Consequently, the larger grain contacts operational in these latter, operate within the same temperature range to larger crystallite sizes in the sintered pellets. Signature of such larger crystallite sizes is visible as much sharper diffraction lines in the Al-doped compared to Al-free samples (Fig. 7b and a, respectively).

The differences observed in the evolution of the density and of the grain growth between the Al-doped samples and the pure ones might be also related to the higher presence of smaller particles in the Al-containing powder. Indeed, the presence of smaller round-shaped particles may also enhance the effectiveness of the reactivity in particular at high density ranges (>85%) where the pores-size to grain-size ratio is increased for the former.[49] It should be noted that the sintering starts from room temperature in both cases (Fig. 6b). This fact is not commonly shown in the literature, where the shrinkage processes usually start between 300 °C and 500 °C at an applied pressure of 50 MPa.[4,28,50,51] It can be understood as a consequence of the higher pressure used in this work (100 MPa), as confirmed by the work of Kinemuchi et al.,[48] who report a density higher than 90% at temperatures from 200 °C when working at a pressure of 500 MPa. On the other hand, the particle size might also play a role in the densification mechanisms of SPS, since the breakdown voltage is more easily reached in nanometer-sized particles and, as a consequence, the densification can occur at lower temperatures.[49] In our case, the similar thickness of the platelets of both pure and Al-doped powders (~10–20 nm) could also be responsible for the early activation of the densification processes following a similar evolution of the shrinkage at lower temperatures in both cases (Fig. 6b).

Finally, the influence of the obtained texture on the measured properties (S, ρ, and κ) is shown in Fig. 13. According to the relatively weak texture strengths and types of our samples, we do not expect an anisotropic influence on the transport properties as significant as that reported by other authors,[32,33] where higher carrier mobilities were found in the c-direction.[32,33] In those works, the crystallographic orientation was claimed to be the origin of such anisotropy. However, the same works also reported non-isotropic grain shapes that were not taken into consideration in the discussion of the results (elongated

grains along the applied magnetic field, that is, perpendicularly to *c*-direction). A recent study by Han et al.[52] on the effect of the morphology on the thermoelectric properties show similar results to those of Kaga et al.,[32] not only in the carrier mobility, but also in the thermal conductivity. In this case, Han et al.[52] conclude that such effects are mainly given by the morphology of the grains due to grain boundary scattering. This conclusion agrees with our results, meaning that the low anisotropic influence on the thermoelectric properties is not due to a weak crystallographic texture of the samples. The isotropic grains obtained after densification do not increase the number of grain boundaries in some special macroscopic direction, which supports the high importance of the morphology of the grains to understand its thermoelectric properties in dense ZnO samples.

With respect to the Seebeck coefficient results (Fig. 13b), there is a general agreement among those of Kaga et al.,[32] the results shown by Han et al.,[52] and ours, showing no dependency on the crystalline orientation. However, the differences in the absolute value of the Seebeck coefficient point to a difference in the oxidation state that might have an influence in the anisotropy observed in the electrical resistivity. In any case, it is important to remark that the doping level used in this work is 0.3%, which is the solubility limit of Al in ZnO, while Kaga et al.[32] work with an Al doping of 2% which leads to the presence of secondary phases not always observed by XRD. Regarding the thermal conductivity, the reported data point to a weak or negligible[53] influence of the intrinsic crystal anisotropy contribution at room temperature. Our data exhibit a ratio $\kappa_{Para}/\kappa_{Perp}$ near 1, where the sub-indexes correspond to the κ measured in the parallel and perpendicular to P_{SPS} direction, respectively. This result is also consistent with the analysis of Han et al.[52] of the thermal conductivity of ZnO. The authors also explain the anisotropy of the thermal conductivity as a direct consequence of the grain boundaries distribution. This feature is a great advantage in applications whose anisotropy may induce constraints and limitations during the process. Alignment of platelet grains with specific crystallographic orientation must be then taken into account more carefully so new ceramics with specific microstructures and textures can be produced with specific properties.

5. Conclusions

Pure and Al-doped ZnO nanoparticles have been synthesized by co-precipitation and densified by Spark Plasma Sintering. A sintering mechanism associated to a specific grain growth has been proposed in both powders (pure and Al-doped). Differences in the densification process and in the resulting texture are evidenced due to the different arrangements observed in the platelet-like particles of the starting powders. The presence of flower-like structures in the pure ZnO starting powder especially hinders the densification and texture. The absence of such structures in the Al-doped samples makes the stacking of platelets easier, leading to higher densities at a lower temperature and higher texture degree than in the case of the pure samples. Interestingly, the microstructure is found to be isotropic which is quite unusual in oxide ceramic with anisotropic precursor powders. The influence of the intrinsic crystals anisotropy on the resulting macroscopic thermoelectric and transport properties seems to be small (for ρ) or even negligible (for S and κ), probably due to the isotropic morphology of the grains.

Acknowledgements

The authors thank Dr S. Marinel, Dr T. Barbier, and Dr P. Lemoine for fruitful discussions. Technical assistance from Mr F.-X. Lefevre and Mr J. Lecourt is also acknowledged.

The authors acknowledge ADEME (Agence de l'Environnement et de la Maîtrise de l'Energie) and TOTAL for the financial support (6th AMI ADEME-TOTAL, Project SONATE (DS2748)).

The authors warmly thank the Conseil Régional Basse-Normandie and European FEDER for funding LL's Chair of Excellence "Analyze Combinée" (Project 2711/33302, FED 1/12/127).

References

1. Özgür Ü, Alivov YI, Liu C, Teke A, Reshchikov MA, Doğan S, et al. A comprehensive review of ZnO materials and devices. *J Appl Phys* 2005;**98**:041301.
2. Pearton SJ, Norton DP, Ip K, Heo YW, Steiner T. Recent progress in processing and properties of ZnO. *Prog Mater Sci* 2005;**50**:293–340.
3. Klingshirn C. ZnO: materials, physics and applications. *Chem Phys Chem* 2007;**8**:782–803.
4. Schwarz S, Thron AM, Rufner J, Benthem Kv, Guillon O. Low temperature sintering of nanocrystalline zinc oxide: effect of heating rate achieved by field assisted sintering/spark plasma sintering. *J Am Ceram Soc* 2012;**95**:2451–7.
5. Loh L, Dunn S. Recent progress in ZnO-based nanostructured ceramics in solar cell applications. *J Nanosci Nanotechnol* 2012;**12**:8215–30.
6. Jose R, Thavasi V, Ramakrishna S. Metal oxides for dye-sensitized solar cells. *J Am Ceram Soc* 2009;**92**:289–301.
7. Guilmeau E, Maignan A, Martin C. Thermoelectric oxides: effect of doping in delafossites and zinc oxide. *J Electron Mater* 2009;**38**:1104–8.
8. Ohtaki M, Tsubota T, Eguchi K, Arai H. High temperature thermoelectric properties of $(Zn_{1-x}Al_x)O$. *J Appl Phys* 1996;**79**:1816–8.
9. Park K, Ko KY. Effect of TiO_2 on high-temperature thermoelectric properties of ZnO. *J Alloys Compd* 2007;**430**:200–4.
10. Berardan D, Byl C, Dragoe N. Influence of the preparation conditions on the thermoelectric properties of Al-doped ZnO. *J Am Ceram Soc* 2010;**93**:2352–8.
11. Katsuyama S, Takagi Y, Ito M, Majima K, Nagai H, Sakai H, et al. Thermoelectric properties of $(Zn_{1-y}\ Mg_y)_{1-x}Al_xO$ ceramics prepared by the polymerized complex method. *J Appl Phys* 2002;**92**:1391–8.
12. Ohtaki M, Araki K, Yamamoto K. High thermoelectric performance of dually doped ZnO ceramics. *J Electron Mater* 2009;**38**:1234–8.
13. Park K, Seong JK, Kim GH. NiO added $Zn_{1-x}Ni_xO$ $(0 \le x \le 0.05)$ for thermoelectric power generation. *J Alloys Compd* 2009;**473**:423–7.
14. Colder H, Guilmeau M, Harnois C, Marinel S, Retoux R, Savary E. Preparation of Ni-doped ZnO ceramics for thermoelectric applications. *J Eur Ceram Soc* 2011;**31**:2957–63.
15. Doggett B, Chakrabarti S, O'Haire R, Meaney A, McGlynn E, Henry MO, et al. Electrical characterization of phosphorous doped ZnO thin films grown by pulsed laser deposition. *Superlattices Microstruct* 2007;**42**:74–8.
16. Panigrahy B, Bahadur D. P-type phosphorous doped ZnO nanostructures: an electrical, optical, and magnetic properties study. *RSC Adv* 2012;**2**:6222–7.

17. Badev A, Marinel S, Heuguet R, Savary E, Agrawal D. Sintering behaviour and non-linear properties of ZnO varistors processed in microwave electric and magnetic fields. *Acta Mater* 2013;**61**:7849–58.
18. Wang ZL. ZnO nanowire and nanobelt platform for nanotechnology. *Mater Sci Eng Rep* 2009;**64**:33–71.
19. Djurisic AB, Ng AMC, Chen XY. ZnO nanostructures for optoelectronics: materials properties and device applications. *Prog Quantum Electr* 2010;**34**:191–259.
20. Ye C, Fang X, Hao Y, Teng X, Zhang L. Zinc oxide nanostructures: morphology derivation and evolution. *J Phys Chem B* 2005;**109**:19758–65.
21. Wang ZL, Kong XY, Ding Y, Gao P, Hughes WL, Yang R, et al. Semiconducting and piezoelectric oxide nanostructures induced by polar surface. *Adv Funct Mater* 2004;**14**:943–56.
22. Wang ZL. Zinc oxide nanostructures: growth, properties and applications. *J Phys: Condens Matter* 2004;**16**:R829.
23. Giovannelli F, Rajonson G, Wolfman J, Delorme F. Synthesis of ZnO microwires and tetrapods by optical furnace. *Mater Lett* 2013;**107**:194–6.
24. Xiang B, Wang P, Zhang X, Dayeh SA, Aplin DPR, Soci C, et al. Rational synthesis of p-Type zinc oxide nanowire arrays using simple chemical vapor deposition. *Nano Lett* 2007;**7**:323–8.
25. Zhou X, Ye Z, Chen F, Xu W, Miao Y, Huang J, et al. Growth of phosphorus doped p-type ZnO thin films by MOCVD. *Chin J Semicond* 2006;**27**:91–5.
26. Abutaha AI, Sarath Kumar SR, Alshareef HN. Crystal orientation dependent thermoelectric properties of highly oriented aluminium-doped zinc oxide thin films. *Appl Phys Lett* 2013;**102**:053507.
27. Manzano CV, Alegre D, Caballero-Calero O, Alén B, Martín-González MS. Synthesis and luminescence properties of electrodeposited ZnO films. *J Appl Phys* 2011;**110**:043538.
28. Langer J, Hoffman MJ, Guillon O. Electric field-assisted sintering and hot pressing of semiconductive zinc oxide. *J Am Ceram Soc* 2011;**94**:2344–53.
29. Munir ZA, Anselmi-Tamburini U, Ohyanagi M. The effect of electric field and pressure on the synthesis and consolidation of materials: a review of the spark plasma sintering method. *J Mater Sci* 2006;**41**:763–77.
30. Zhang X-Y, Chen Z-W, Qi Y-P, Feng Y, Zhao L, Qi L, et al. Ab initio comparative study of zincblende and wurzite ZnO. *Chin Phys Lett* 2007;**24**:1032–4.
31. Ding Y, Wang ZL. Zinc-blende ZnO and its role in nucleating wurzite tetrapods and twinned nanowires. *Appl Phys Lett* 2007;**90**:153510.
32. Kaga H, Kinemuchi Y, Tanaka S, Makiya A, Kato Z, Uematsu K, et al. Preparation and thermoelectric property of highly oriented Al-doped ZnO ceramics by a high magnetic field. *Jpn J Appl Phys* 2006;**45**:L1212–4.
33. Ning JL, Jiang DM, Kim KH, Shim KB. Influence of texture on electrical properties of ZnO ceramics prepared by extrusion and spark plasma sintering. *Ceram Int* 2007;**33**:107–14.
34. Uchikoshi T, Suzuki TS, Sakka Y. Fabrication of c-axis oriented zinc oxide by electrophoretic deposition in rotating magnetic field. *J Eur Ceram Soc* 2010;**30**:1171–5.
35. Suvaci E, Özer Ö. Processing of textured zinc oxide varistors via templated grain growth. *J Eur Ceram Soc* 2005;**25**:1663.
36. Giovannelli F, Ngo Ndimba A, Diaz-Chao P, Motelica-Heino M, Raynal PI, Autret C, et al. Synthesis of Al doped ZnO nanoparticles by aqueous coprecipitation. *Powder Technol* 2014;**262**:203–8.
37. Gratuze B, Blet-Lemarquand M, Barrandon JN. Mass spectrometry with laser sampling: a new tool to characterize archaeological materials. *J Radioanal Nucl Chem* 2001;**247**(3):645–56.
38. Aries S, Motellica-Heino M, Freydier R, Grezes T, Polvé M. Direct determination of lead isotope ratios by laser ablation-inductively coupled plasma-quadrupole mass spectrometry in lake sediment samples. *J Geostand Geoanal* 2001;**25**:387–98.
39. Motelica-Heino M, Donard OFX. Comparison of UV and IR laser ablation ICP-MS on silicate reference materials and implementation of normalisation factors for quantitative measurements. *Geostandard Newslett* 2001;**25**:345–59.
40. Morales M, Chateigner D, Lutterotti L, Ricote J. X-ray combined QTA using a CPS applied to a ferroelectric ultrastructure. *Mater Sci Forum* 2002;**408–412**:113–8.
41. Chateigner D. *Combined analysis*. London: Ed. Wiley-ISTE; 2010. p. 496.
42. Lutterotti L, Matthies S, Wenk HR. In: Spunar JA, editor. *MAUD (material analysis using diffraction): a user friendly Java program for Rietveld Texture Analysis and more*. Ottawa: National Research Council of Canada; 1999. p. 1599–604.
43. Grazulis S, Chateigner D, Downs RT, Yokochi AFT, Quiros M, Lutterotti L, et al. Crystallography open database – an open-access collection of crystal structures. *J Appl Crystallogr* 2009;**42**(4):726.
44. Sondegaard M, Bojesen ED, Borup KA, Christensen S, Christensen M, Iversen BB. Sintering and annealing effects of ZnO microstructure and thermoelectric properties. *Acta Mater* 2013;**61**:3314–23.
45. He M, Jiu H, Liu Y, Tian Y, Li D, Sun Y, et al. Controllable synthesis of ZnO microstructures with morphologies from rods to disks. *Mater Lett* 2013;**92**:154–6.
46. Tomakin M. Structural and optical properties of ZnO and Al-doped ZnO microrods obtained by spray pyrolysis method using different solvents. *Superlattices Microstruct* 2012;**51**:372–80.
47. Serier H, Gaudon M, Ménétrier M. Al-doped ZnO powdered materials: Al solubility limit and IR absorption properties. *Solid State Sci* 2009;**11**:1192–7.
48. Kinemuchi Y, Mikami M, Kobayashi K, Watari K, Hotta Y. Thermoelectric properties of nanograined ZnO. *J Electron Mater* 2010;**39**:2059.
49. Chaim R. Densification mechanisms in spark plasma sintering of nanocrystalline ceramics. *Mater Sci Eng* 2007;**443**:25.
50. Ma N, Li J-F, Zhang BP, Lin YH, Ren LR, Chen GF. Microstructure and thermoelectric properties of $Zn_{1-x}Al_xO$ ceramics fabricated by spark plasma sintering. *J Phys Chem Solids* 2010;**71**:1344–9.
51. Nam WH, Lim YS, Choi S-M, Seo W-S, Lee JY. High temperature charge transport and thermoelectric properties of a degenerately Al-doped ZnO nanocomposite. *J Mater Chem* 2012;**22**:14633.
52. Han L, Nong NV, Zhang W, Hung LT, Holgate T, Tashiro K, et al. Effects of morphology on the thermoelectric properties of Al-doped ZnO. *RSC Adv* 2014;**4**:12353.
53. Slack GA. Thermal conductivity of II–IV compounds and phonon scattering by Fe^{2+} impurities. *Phys Rev B* 1972;**6**:3791.